

Reaching the Continuum Limit in Finite-Temperature *Ab Initio* Field-Theory Computations in Many-Fermion Systems

Yuan-Yao He,^{1,2} Hao Shi,¹ and Shiwei Zhang^{1,2}

¹*Center for Computational Quantum Physics, Flatiron Institute, New York, New York 10010, USA*

²*Department of Physics, College of William and Mary, Williamsburg, Virginia 23187, USA*



(Received 17 June 2019; published 24 September 2019)

Finite-temperature grand-canonical computations based on field theory are widely applied in areas including condensed matter physics, ultracold atomic gas systems, and the lattice gauge theory. However, these calculations have computational costs scaling as N_s^3 with the size of the lattice or basis set, N_s . We report a new approach based on systematically controllable low-rank factorization that reduces the scaling of such computations to $N_s N_e^2$, where N_e is the average number of fermions in the system. In any realistic calculations aiming to describe the continuum limit, N_s/N_e is large and needs to be extrapolated effectively to infinity for convergence. The method thus fundamentally changes the prospect for finite-temperature many-body computations in correlated fermion systems. Its application, in combination with frameworks to control the sign or phase problem as needed, will provide a powerful tool in *ab initio* quantum chemistry and correlated electron materials. We demonstrate the method by computing exact properties of the two-dimensional Fermi gas with zero-range attractive interaction as a function of temperature in both the normal and superfluid states.

DOI: [10.1103/PhysRevLett.123.136402](https://doi.org/10.1103/PhysRevLett.123.136402)

Computations are playing an increasingly important role in addressing the fundamental challenges of understanding strong correlations in interacting quantum systems. Understandably, a major part of the development and application efforts in both physics and chemistry has focused on ground-state properties. However, experimental conditions are always at finite temperatures, where often rich and new properties can be revealed [1–4]. One example is the rapid development in the area of experiments with ultracold atoms, where temperature plays a crucial role and very precise measurements of properties are often possible with exquisite control over interaction strengths, environments, etc., [5,6]. Accurate computations of thermodynamic properties allow direct comparisons with experiments, but they are challenging because of the presence of strong coupling and thermal fluctuations. A second example is in strongly correlated materials, including high-temperature superconductors [7,8], where some of the outstanding and most interesting physics questions concern finite-temperature properties [9].

A common finite-temperature formalism is based on field theory in which the thermodynamic properties are computed as path integrals in field space, with the many-dimensional integration evaluated by Monte Carlo methods [10]. This has become a key technique for many-body finite-temperature computations, which is widely applied in several fields of physics [11–20]. For example, many of the sign-problem-free computations in lattice models in condensed matter, as well as in Fermi gas and the optical lattices of ultracold atoms, have been performed this way.

For general Hamiltonians (for instance, the doped Hubbard model or realistic electronic Hamiltonians in solids or molecules), a constraint can be applied to control the sign or phase problem. This framework has been referred to as the constrained-path auxiliary-field quantum Monte Carlo (AFQMC) method [21–29]. Even with simple trial wave functions to impose an approximate constraint, it has been shown to be very accurate and has been applied widely in ground-state calculations. Finite-temperature generalization of the approach has also been developed [30–33].

These finite-temperature calculations all have a computational complexity of $\mathcal{O}(N_s^3)$ [34] because they are formulated in the grand-canonical ensemble to analytically evaluate the fermion trace along each path in auxiliary-field space, leading to determinants with dimension N_s . In the majority of applications (for example, dilute Fermi gas and all *ab initio* real material simulations), it is necessary to reach the continuum (large lattice or complete basis set) limit in order to obtain realistic results. One must take $N_s \rightarrow \infty$ while keeping the average number of fermions N_e fixed (at the targeted number of electrons in the molecule or cluster, or in the supercell). In contrast, all ground-state calculations, which are formulated in a canonical ensemble and only need to retain occupied orbitals along the path in field space, scale as $\mathcal{O}(N_s N_e^2)$ [35]. The ratio N_s/N_e is often $\mathcal{O}(10\text{--}100)$ or larger for realistic calculations. The discrepancy of $(N_s/N_e)^2$ in computational cost can render calculations inaccessible at low, or even modest, temperatures when the corresponding ground-state calculations can be performed straightforwardly. This poses a

fundamental obstacle for finite-temperature studies in interacting fermion systems.

We address this problem in the present Letter, introducing a new method that allows finite-temperature computations to be performed with complexity $\mathcal{O}(N_s N_e^2)$, with no loss of accuracy. We demonstrate the approach within the framework of sign-problem-free determinantal quantum Monte Carlo (DQMC) calculations in the two-dimensional (2D) dilute Fermi gas with contact interaction, which has attracted intense experimental interest. The algorithm yields speedups of several orders of magnitude over the standard approach, and it allows computations of exact thermodynamic properties in the continuum. This adds a new dimension in our computational repertoire; for example, it allows direct *ab initio* computations of the superfluid state in strongly interacting Fermi gases and investigations of the corresponding phase transitions.

For concreteness in describing the algorithm, and to specify the computational details for the 2D dilute Fermi gas, we use the attractive Hubbard model on a square lattice:

$$\hat{H} = \sum_{\mathbf{k}\sigma} \varepsilon_{\mathbf{k}} c_{\mathbf{k}\sigma}^\dagger c_{\mathbf{k}\sigma} - \mu \sum_{\mathbf{i}\sigma} \hat{n}_{\mathbf{i}\sigma} + U \sum_{\mathbf{i}} \hat{n}_{\mathbf{i}\uparrow} \hat{n}_{\mathbf{i}\downarrow}, \quad (1)$$

where $\varepsilon_{\mathbf{k}} = 2t(2 - \cos k_x - \cos k_y)$, $\sigma (= \uparrow \text{ or } \downarrow)$ denotes spin, and $\hat{n}_{\mathbf{i}\sigma} = c_{\mathbf{i}\sigma}^\dagger c_{\mathbf{i}\sigma}$ is the density operator. The periodic supercell is represented by a lattice of size $N_s = L^2$, with corresponding momentum k_x (and k_y) defined in units of $2\pi/L$. The chemical potential μ/t is tuned to target the desired number of particles in the supercell, $N_e = N_\uparrow + N_\downarrow$, defining a lattice density of $n = N_e/N_s$. The interaction strength U/t is uniquely determined by $\log(k_F a)$ [35], i.e., the ratio of the two-particle scattering length to the average interparticle spacing (given by the Fermi wave vector k_F). We will measure energies in units of the Fermi energy $E_F = 2\pi n t$ and temperatures in units of $T_F \equiv E_F/k_B$.

The partition function $Z = \text{Tr}(e^{-\beta\hat{H}})$, after imaginary-time discretization $\beta = \Delta\tau M$; the Trotter decomposition; and the Hubbard-Stratonovich transformation, can be written as [33]

$$Z \simeq \int P(\mathbf{X}) \prod_{\sigma=\uparrow,\downarrow} \det(\mathbf{1}_{N_s} + \mathbf{B}_M^\sigma \mathbf{B}_{M-1}^\sigma \cdots \mathbf{B}_2^\sigma \mathbf{B}_1^\sigma) d\mathbf{X}, \quad (2)$$

where $\mathbf{X} = \{\mathbf{x}_1, \mathbf{x}_2, \dots, \mathbf{x}_M\}$ is a path in auxiliary-field space, and $P(\mathbf{X})$ is a probability density function. The auxiliary fields at each time slice, $\mathbf{x}_\ell = \{x_{i,\ell}\}$, can be either continuous [e.g., $P(\mathbf{X})$ is a Gaussian] or discrete fields (as we adopt below for our Fermi gas calculations); in which case, the integral becomes a sum. The “ \simeq ” indicates the Trotter error, which can be extrapolated away with calculations using several $\Delta\tau$ values. The one-body propagator \mathbf{B}_ℓ^σ depends on \mathbf{x}_ℓ , and it is an $N_s \times N_s$ matrix. The paths \mathbf{X} are sampled according to the integrand in Eq. (2) for example by Metropolis Monte Carlo in DQMC or by a

branching random walk of fixed length M in constrained-path AFQMC [33].

To describe our algorithm, we introduce the notations $\mathbf{R} = \mathbf{B}_\ell^\sigma \cdots \mathbf{B}_2^\sigma \mathbf{B}_1^\sigma$ and $\mathbf{L} = \mathbf{B}_M^\sigma \mathbf{B}_{M-1}^\sigma \cdots \mathbf{B}_{\ell+1}^\sigma$, where ℓ is an arbitrary time slice along the path. The key components of DQMC and AFQMC calculations include propagation, numerical stabilization, evaluations of the ratios or the derivative of the integrand with respect to \mathbf{x}_ℓ during updates, and measurements. These procedures all involve operations of the matrix products \mathbf{L} and \mathbf{R} . For example, the update and measurements at $\tau = \ell\Delta\tau$ require the equal-time single-particle Green’s function $\mathbf{G}^\sigma(\tau, \tau) \equiv \{\langle c_{i\sigma} c_{j\sigma}^\dagger \rangle_\tau\} = (\mathbf{1}_{N_s} + \mathbf{R}\mathbf{L})^{-1}$. Because of the manipulation of these matrices and the computation of the determinant, the overall computational complexity scales as $\mathcal{O}(N_s^3)$ [34] (with a proportionality factor containing the imaginary-time length M). This basic structure is depicted in Fig. 1(a).

The matrices can be written in factorized forms [for example, using the column-pivoted QR algorithm to perform \mathbf{UDV} decompositions (see, e.g., Ref. [33])] to obtain $\mathbf{R} = \mathbf{U}_R \mathbf{D}_R \mathbf{V}_R$ and $\mathbf{L} = \mathbf{V}_L \mathbf{D}_L \mathbf{U}_L$, where \mathbf{D}_R and \mathbf{D}_L are diagonal matrices with positive elements in descending order and \mathbf{U}_R , \mathbf{U}_L , \mathbf{V}_R , and \mathbf{V}_L are $N_s \times N_s$ matrices, which are used in standard methods as part of the procedure to keep numerical stability [33,34,36]. The diagonal elements of \mathbf{D}_L and \mathbf{D}_R typically span an enormous scale (e.g., 10^{+100} – 10^{-100}), which is controlled by the independent-particle spectrum, interaction strength, and inverse temperature. We now introduce a threshold ϵ to perform truncations on them in computing \mathbf{R} and \mathbf{L} . Contributions from the elements of \mathbf{D}_R and \mathbf{D}_L smaller than ϵ will be bounded and can be made smaller than numerical noise if the truncation threshold ϵ is sufficiently

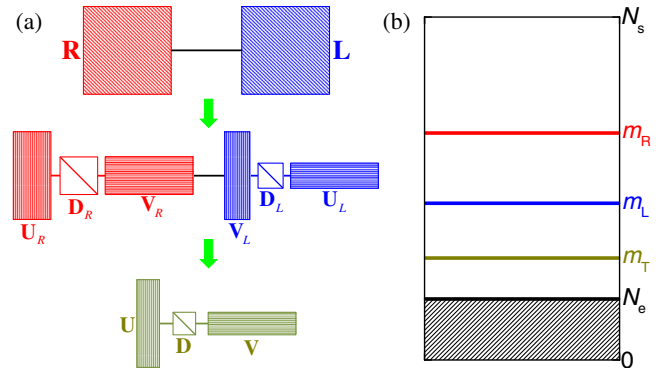


FIG. 1. Schematic illustration of the decomposition and truncations along a field path. The path is separated at τ into two parts, \mathbf{L} and \mathbf{R} , which are $N_s \times N_s$ matrices of propagator products [top row of Fig. 1(a)]. They are factorized and truncated with controlling dimensions m_L and m_R , respectively, which change dynamically as τ evolves in the sampling [Fig. 1(b) and the second row of Fig. 1(a)]. A further factorization can be performed after \mathbf{L} and \mathbf{R} are combined [bottom row in Fig. 1(a)], leading to a further truncation with dimension m_T .

small. Thus, ϵ is a parameter that we can tune to control the numerical precision of the calculation. Suppose the number of elements in \mathbf{D}_R larger than ϵ is m_R ; then, \mathbf{U}_R , \mathbf{D}_R , and \mathbf{V}_R are effectively $N_s \times m_R$, $m_R \times m_R$, and $m_R \times N_s$ matrices. Similarly, we have a truncation dimension m_L for \mathbf{D}_L and a low-rank approximation for \mathbf{L} . The truncations are illustrated in Fig. 1. We can then decompose $\mathbf{R}\mathbf{L} = \mathbf{U}\mathbf{D}\mathbf{V}$ and perform an additional truncation on \mathbf{D} , with truncation dimension m_T , as shown in the bottom row of Fig. 1(a). We should note that, methodologically, the above idea fits into a theme of low-rank factorizations that have found broad applications in very different contexts in physics and chemistry (e.g., density matrix renormalization group [37] and tensor hyper contraction of quantum chemical Hamiltonians [38]).

With the new formalism, updating all the auxiliary fields on a single imaginary-time slice costs $\mathcal{O}(N_s m_T^2)$ to calculate the force bias [35] and $\mathcal{O}(m_T^3)$ to calculate the ratio of the determinant in Eq. (2), applying $\det(\mathbf{1}_{N_s} + \mathbf{U}\mathbf{D}\mathbf{V}) = \det(\mathbf{1}_{m_T} + \mathbf{D}\mathbf{V}\mathbf{U})$. Propagation along the path (i.e., moving ℓ to the left or right) becomes a propagation on \mathbf{U}_R and \mathbf{U}_L , which can be achieved with $\mathcal{O}(N_s m_{R,L} \log N_s)$ scaling using FFT and locality of the interaction in Eq. (1). For a single numerical stabilization, the complexity is also lowered to $\mathcal{O}(N_s m_{R,L}^2)$ because we are dealing with \mathbf{U}_R and \mathbf{U}_L matrices. For measurements, we compute the Green's function as

$$\mathbf{G}^\sigma(\tau, \tau) = (\mathbf{1}_{N_s} + \mathbf{U}\mathbf{D}\mathbf{V})^{-1} = \mathbf{1}_{N_s} - \mathbf{U}\mathbf{D}(\mathbf{1}_{m_T} + \mathbf{V}\mathbf{U}\mathbf{D})^{-1}\mathbf{V}.$$

In the calculations, m_R , m_L , and m_T evolve dynamically as we carry out the truncations following each numerical stabilization procedure. At the start and end of a sweep, m_R or m_L is close to N_s ; but, away from the ends, they rapidly

decay, as illustrated in Fig. 2(a). The “truncation efficiency,” defined as $\eta_{L,R,T} = (N_s - m_{L,R,T}) / (N_s - N_\sigma)$ (with $N_\sigma = N_e/2$), remains over 90%, except for small portions at the ends. The computational complexity is dominated by the main part of the path in the middle, which scales as $\mathcal{O}(N_s m_T^2)$, and the overall m_T is small across the entire path. In standard DQMC, lowering the temperature makes the calculation progressively more challenging; as $T \rightarrow 0$, the computational efficiency reaches its worst in comparison with the ground-state method. In our new method, m_T approaches N_e as T is lowered, and the algorithm restores the same computational complexity as the ground-state projection approach. At higher temperatures, m_T increases. In the example in Fig. 2(a), m_T is ~ 1.3 times and ~ 2.5 times the ground-state value at $T/T_F = 0.055$ and 0.274 , respectively; but, even in the latter, a speedup of ~ 30 is achieved. As mentioned earlier, the closer to the continuum limit, the larger the speedup because m_T only depends on physical parameters such as N_e and T , and it will change little as N_s is increased.

As shown in the inset in Fig. 2(a), the truncation error is invisible even with an aggressive truncation threshold of $\epsilon = 10^{-3}$ [39]. We tested that these results are not sensitive to the temperature. We have also carried out simulations for different interaction strengths ($U/t = -1$ and -6) and obtained similar results. Moreover, these results hold generally for different Hubbard-Stratonovich transformations, e.g., total density or spin- s_z channels for Eq. (1) [12].

The speedup of our new algorithm over the current state of the art is illustrated in Fig. 2(b). The main figure displays the speedup vs the linear dimension of the lattice for 2D Fermi gas system. The speedups fit a fourth-order polynomial well for L up to 30, which is consistent with the earlier conclusion of $(N_s/m_T)^2$ from computational

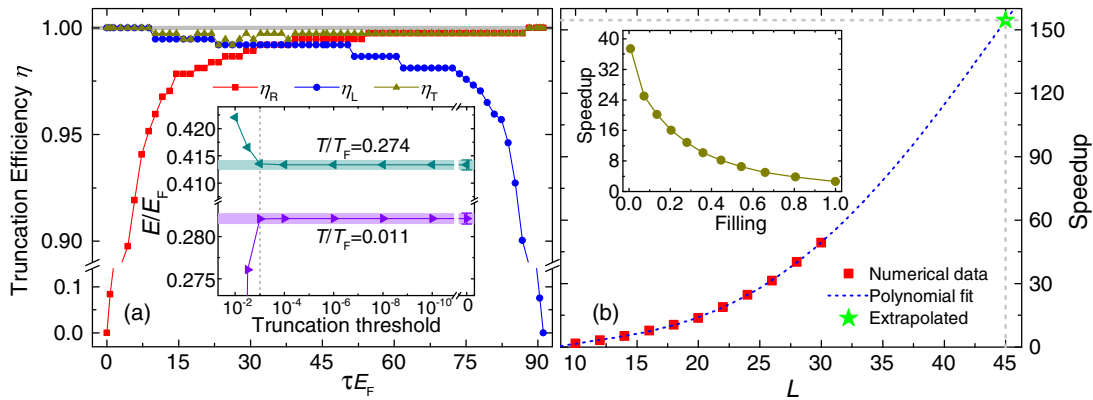


FIG. 2. Efficiency and accuracy of the factorization and truncation, and computational scaling and speedup. In Fig. 2(a), truncation efficiency $\eta_{L,R,T}$ (see text) is shown for a system with $L = 20$, $N_e = 58$, $U/t = -3$, and $T/T_F = 0.011$. Note the zoomed-in vertical scale for $\eta > 0.9$. The inset shows the computed total energy per particle vs the truncation threshold ϵ for two temperatures: $T/T_F = 0.274$ ($\beta t = 4$) and $T/T_F = 0.011$ ($\beta t = 100$). The truncation error can be deduced from comparison with the result at $\epsilon = 0$, which shows the full result (no truncation), with typical final statistical errors indicated by the shading. In Fig. 2(b), the main graph shows speedup vs lattice linear dimension for $\log(k_F a) = 4.346574$, $N_e = 58$, and $T/T_F = 1/32$; whereas the inset presents speedup vs lattice density for $L = 32$, $U/t = -3$, and $\beta t = 32$.

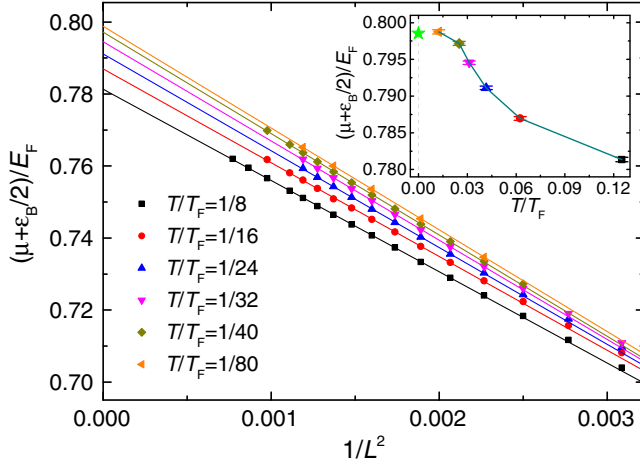


FIG. 3. Equation of state at $\log(k_F a) = 4.346574$ with $N_e = 58$ as a function of temperature. The main graph plots $(\mu + \varepsilon_B/2)/E_F$ vs inverse lattice size, as well as linear fits in the asymptotic regime. Numerical uncertainties are smaller than the symbol size. The inset presents the corresponding results at the continuum limit. The ground-state result is indicated (green pentagram, with error bar comparable to the symbol size, from Ref. [35]).

complexity. The speedup is around 50 at $L = 30$, and it extrapolates to ~ 150 for $L = 45$, which takes five days of computing (on 40 Skylake cores) with the new algorithm, and which would have required over two years of computing with the standard algorithm using comparable resources. The inset illustrates the speedup vs filling by tuning the chemical potential in the Hubbard model. Large speedups are seen at low density, as expected. Even at half-filling, a speedup of 2.65 is achieved.

We next apply the method to the spin-balanced uniform 2D Fermi gas with a zero-range attractive interaction. Major experimental efforts are being devoted to this and related systems [40–46], which offer opportunities for highly controllable and clean experiments in a strongly interacting 2D quantum system. The ground-state properties of this system have been studied by various quantum Monte Carlo methods [35,47,48], whereas finite- T *ab initio* computations to date have been mostly limited to the normal state [20]. The algorithmic advances presented in this Letter allow exact computations to reach much larger lattices and lower T 's, which add a new dimension to our computational and theoretical capabilities, and will help calibrate and guide experiments. Here, as an illustration of the method, we present examples on the equation of state (EOS) and pairing properties.

In Fig. 3, we present the results of the EOS at the interaction strength $\log(k_F a) = 4.346574$, which is on the BCS side. As shown in the main plot, $(\mu + \varepsilon_B/2)/E_F$ (note the binding energy $\varepsilon_B = 4\hbar^2/ma^2e^{2\gamma}$ with Euler's constant $\gamma = 0.57721$) has perfect linear scaling with $1/L^2$ at large L for all the temperatures. After extrapolation to the continuum limit, $(\mu + \varepsilon_B/2)/E_F$ converges to the ground-state

result when $T \rightarrow 0$, as shown in the inset. Our results indicate that the small discrepancy between the experiment [43] and ground-state results [35] is consistent with finite- T effects, which can now be better understood as experimental resolution improves.

We have also determined the pairing wave function and condensate fraction by computing the zero-momentum spin-singlet pairing matrix: $\mathbf{M}_{\mathbf{k}\mathbf{k}'} = \langle \Delta_{\mathbf{k}}^+ \Delta_{\mathbf{k}'} \rangle - \delta_{\mathbf{k}\mathbf{k}'} \langle c_{\mathbf{k}\uparrow}^+ c_{\mathbf{k}\uparrow} \rangle \langle c_{-\mathbf{k}\downarrow}^+ c_{-\mathbf{k}\downarrow} \rangle$ with $\Delta_{\mathbf{k}}^+ = c_{\mathbf{k}\uparrow}^+ c_{-\mathbf{k}\downarrow}^+$. Its leading eigenvalue divided by $N_e/2$ is identified as the condensate fraction. The corresponding eigenvector gives the pairing wave function $\phi_{\uparrow\downarrow}(\mathbf{k})$. The results are shown in Fig. 4 for $\log(k_F a) = 0.50$ in the strongly interacting crossover regime. The mean-field condensate fraction, which is dramatically different from the exact result, illustrates the strong correlation effect. The mean-field result also indicates that residual finite-size effects are negligible, although they could be larger in the many-body result, especially for small values at the tail. At high temperatures, the pairing wave function is more extended in momentum space, and the condensate fraction is tiny. As T lowers, the pairing wave function peaks more at the Fermi surface, and the condensate fraction increases rapidly. The Berezinskii-Kosterlitz-Thouless (BKT) transition temperature measured experimentally [40] (but, also see discussions in Ref. [49]) is shown in the inset of Fig. 4. It is clear that the new method now makes possible a quantitative comparison with experiments. A more systematic study of the physics of the 2D Fermi gas and the BKT transition will be published separately.

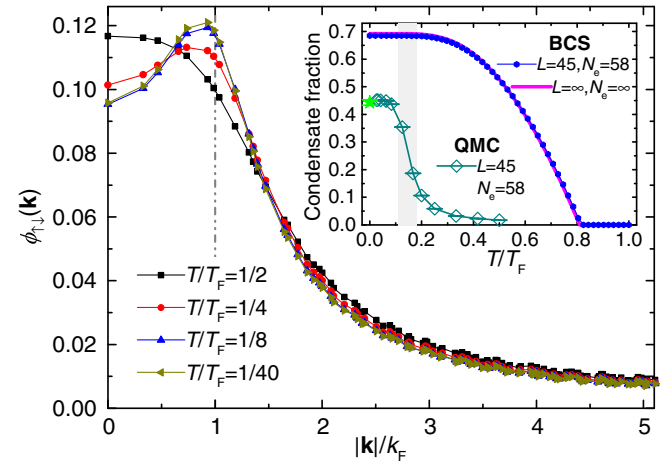


FIG. 4. Spin-singlet pairing wave function in reciprocal space vs $|\mathbf{k}|/k_F$, as well as condensate fraction, for $\log(k_F a) = 0.50$ with $L = 45$ and $N_e = 58$ as a function of temperature. In the main graph, the error bars in $\phi_{\uparrow\downarrow}(\mathbf{k})$ are smaller than the symbol size. The inset shows the condensate fraction from both quantum Monte Carlo (QMC) and mean-field calculations, as well as the exact ground-state result (green pentagram, from Ref. [35]). As a guide, an experimental estimate of T_c/T_F for the BKT transition (from Ref. [40]) is also shown, with the gray shading indicating uncertainty.

We have described the algorithm with some specificity in the context of DQMC for a lattice model. As mentioned, the advances are general and can be applied to many forms of finite-temperature field-theory computations, including mean-field theory. The inclusion of spin-flip terms, such as spin-orbit coupling, can be accommodated straightforwardly [50,51]. In the presence of a sign problem (e.g., repulsive or spin-imbalanced Hubbard-like models), the constrained-path AFQMC framework [30–33] can be used. In that case, \mathbf{L} becomes the trial propagator matrix \mathbf{L}_T , and only \mathbf{R} depends on the path (see Supplemental Material [52]). The low-rank factorizations can be applied in exactly the same way. For electronic Hamiltonians, as in molecules and solids, a phase problem arises and the phaseless approximation [25,32] is needed. The rest of the algorithm is identical to the sign problem case. (For a plane-wave basis [26], one can alternate between Fourier and real space [26], similar to the Hubbard model; and the computational scaling is similar to what we have discussed. For generic basis sets, such as in quantum chemistry, however, the \mathbf{B} 's have a more general structure and the propagation scales as $\mathcal{O}(N_s^2 m_{L,R})$, which means the reduction in computational complexity is one power of N_s/N_e .) The factorization and truncation also apply to bosons and Fermi-Bose mixtures [53]. More broadly, the idea should also be applicable to calculations employing similar formalisms in nuclear shell models [14,18] and lattice QCD [15,54–57].

In summary, we have presented a method to perform finite-temperature field-theoretic calculations of many-fermion systems with computational complexity $\mathcal{O}(N_s N_e^2)$, i.e., linear in lattice (or single-particle basis) size. Such calculations are applied widely, and their fundamental complexity of $\mathcal{O}(N_s^3)$ previously has been a major obstacle for approaching the continuum limit ($N_s/N_e \rightarrow \infty$). We demonstrated the method in 2D strongly interacting Fermi gas, where the continuum limit can be reached via numerically exact calculations with large lattice sizes, even at low temperatures. The method introduced here can be applied to a variety of strongly interacting fermion systems in multiple fields, including ultracold atomic gases, condensed matter and materials, and quantum chemistry.

We thank J. Carlson, P. Dumitrescu, and S. Chandrasekharan for helpful discussions. This work was supported by the NSF (Grant No. DMR-1409510). The Flatiron Institute is a division of the Simons Foundation.

Note added in the proof.—Recently, we became aware of work by C.N. Gilbreth *et al.* [58] which applied model space truncations in the computation of Green's functions.

- [1] A. Damascelli, Z. Hussain, and Z.-X. Shen, *Rev. Mod. Phys.* **75**, 473 (2003).
- [2] O. Fischer, M. Kugler, I. Maggio-Aprile, C. Berthod, and C. Renner, *Rev. Mod. Phys.* **79**, 353 (2007).
- [3] E. J. Mueller, *Rep. Prog. Phys.* **80**, 104401 (2017).
- [4] P. T. Brown, D. Mitra, E. Guardado-Sanchez, R. Nourafkan, A. Reymbaut, C.-D. Hébert, S. Bergeron, A.-M. S. Tremblay, J. Kokalj, D. A. Huse, P. Schauß, and W. S. Bakr, *Science* **363**, 379 (2019).
- [5] I. Bloch, J. Dalibard, and W. Zwerger, *Rev. Mod. Phys.* **80**, 885 (2008).
- [6] L. Tarruell and L. Sanchez-Palencia, *C.R. Phys.* **19**, 365 (2018).
- [7] J. G. Bednorz and K. A. Müller, *Z. Phys. B* **64**, 189 (1986).
- [8] A. Saleem and S. Tajammul Hussain, *J. Surf. Interfaces Mater.* **1**, 97 (2013).
- [9] P. A. Lee, N. Nagaosa, and X.-G. Wen, *Rev. Mod. Phys.* **78**, 17 (2006).
- [10] R. Blankenbecler, D. J. Scalapino, and R. L. Sugar, *Phys. Rev. D* **24**, 2278 (1981).
- [11] D. J. Scalapino and R. L. Sugar, *Phys. Rev. B* **24**, 4295 (1981).
- [12] J. E. Hirsch, *Phys. Rev. B* **28**, 4059 (1983).
- [13] J. E. Hirsch, *Phys. Rev. B* **31**, 4403 (1985).
- [14] Y. Alhassid, *Int. J. Mod. Phys. B* **15**, 1447 (2001).
- [15] S. Chandrasekharan, *Phys. Rev. Lett.* **97**, 182001 (2006).
- [16] S. Chandrasekharan, *Phys. Rev. D* **82**, 025007 (2010).
- [17] E. Huffman and S. Chandrasekharan, *Phys. Rev. D* **96**, 114502 (2017).
- [18] Y. Alhassid, G. Bertsch, C. Gilbreth, and M. Mustonen, *J. Phys. Conf. Ser.* **966**, 012059 (2018).
- [19] S. Jensen, C. N. Gilbreth, and Y. Alhassid, *Eur. Phys. J. Spec. Top.* **227**, 2241 (2019).
- [20] E. R. Anderson and J. E. Drut, *Phys. Rev. Lett.* **115**, 115301 (2015).
- [21] S. Zhang, J. Carlson, and J. E. Gubernatis, *Phys. Rev. Lett.* **74**, 3652 (1995).
- [22] S. Zhang, J. Carlson, and J. E. Gubernatis, *Phys. Rev. B* **55**, 7464 (1997).
- [23] S. Zhang, J. Carlson, and J. E. Gubernatis, *Phys. Rev. Lett.* **78**, 4486 (1997).
- [24] J. Carlson, J. E. Gubernatis, G. Ortiz, and S. Zhang, *Phys. Rev. B* **59**, 12788 (1999).
- [25] S. Zhang and H. Krakauer, *Phys. Rev. Lett.* **90**, 136401 (2003).
- [26] M. Suewattana, W. Purwanto, S. Zhang, H. Krakauer, and E. J. Walter, *Phys. Rev. B* **75**, 245123 (2007).
- [27] C.-C. Chang and S. Zhang, *Phys. Rev. Lett.* **104**, 116402 (2010).
- [28] M. Qin, H. Shi, and S. Zhang, *Phys. Rev. B* **94**, 235119 (2016).
- [29] E. Vitali, H. Shi, A. Chiciak, and S. Zhang, *Phys. Rev. B* **99**, 165116 (2019).
- [30] S. Zhang, *Phys. Rev. Lett.* **83**, 2777 (1999).
- [31] S. Zhang, *Comput. Phys. Commun.* **127**, 150 (2000).
- [32] Y. Liu, M. Cho, and B. Rubenstein, *J. Chem. Theory Comput.* **14**, 4722 (2018).
- [33] Y.-Y. He, M. Qin, H. Shi, Z.-Y. Lu, and S. Zhang, *Phys. Rev. B* **99**, 045108 (2019).
- [34] E. Y. Loh, J. E. Gubernatis, R. T. Scalettar, S. R. White, D. J. Scalapino, and R. L. Sugar, *Int. J. Mod. Phys. C* **16**, 1319 (2005).
- [35] H. Shi, S. Chiesa, and S. Zhang, *Phys. Rev. A* **92**, 033603 (2015).

- [36] S. R. White, D. J. Scalapino, R. L. Sugar, E. Y. Loh, J. E. Gubernatis, and R. T. Scalettar, *Phys. Rev. B* **40**, 506 (1989).
- [37] S. R. White, *Phys. Rev. Lett.* **69**, 2863 (1992); *Phys. Rev. B* **48**, 10345 (1993).
- [38] E. G. Hohenstein, R. M. Parrish, and T. J. Martínez, *J. Chem. Phys.* **137**, 044103 (2012); R. M. Parrish, E. G. Hohenstein, T. J. Martínez, and C. D. Sherrill, *J. Chem. Phys.* **137**, 224106 (2012).
- [39] The comparison of different ϵ vs $\epsilon = +0$ (i.e., the standard algorithm) was done on an identical set of random paths. In practical calculations, the different choices of ϵ would cause the calculations to, in sufficiently long runs, cease being correlated in their random number streams, but they will give statistically compatible results.
- [40] M. G. Ries, A. N. Wenz, G. Zürn, L. Bayha, I. Boettcher, D. Kedar, P. A. Murthy, M. Neidig, T. Lompe, and S. Jochim, *Phys. Rev. Lett.* **114**, 230401 (2015).
- [41] K. Martiyanov, V. Makhalov, and A. Turlapov, *Phys. Rev. Lett.* **105**, 030404 (2010).
- [42] P. A. Murthy, I. Boettcher, L. Bayha, M. Holzmann, D. Kedar, M. Neidig, M. G. Ries, A. N. Wenz, G. Zürn, and S. Jochim, *Phys. Rev. Lett.* **115**, 010401 (2015).
- [43] I. Boettcher, L. Bayha, D. Kedar, P. A. Murthy, M. Neidig, M. G. Ries, A. N. Wenz, G. Zürn, S. Jochim, and T. Enss, *Phys. Rev. Lett.* **116**, 045303 (2016).
- [44] K. Fenech, P. Dyke, T. Pepler, M. G. Lingham, S. Hoinka, H. Hu, and C. J. Vale, *Phys. Rev. Lett.* **116**, 045302 (2016).
- [45] K. Hueck, N. Luick, L. Sobirey, J. Siegl, T. Lompe, and H. Moritz, *Phys. Rev. Lett.* **120**, 060402 (2018).
- [46] P. A. Murthy, M. Neidig, R. Klemt, L. Bayha, I. Boettcher, T. Enss, M. Holten, G. Zürn, P. M. Preiss, and S. Jochim, *Science* **359**, 452 (2018).
- [47] G. Bertaina and S. Giorgini, *Phys. Rev. Lett.* **106**, 110403 (2011).
- [48] L. M. Schonenberg, P. C. Verpoort, and G. J. Conduit, *Phys. Rev. A* **96**, 023619 (2017).
- [49] M. Matsumoto, D. Inotani, and Y. Ohashi, *Phys. Rev. A* **93**, 013619 (2016).
- [50] H. Shi, P. Rosenberg, S. Chiesa, and S. Zhang, *Phys. Rev. Lett.* **117**, 040401 (2016).
- [51] P. Rosenberg, H. Shi, and S. Zhang, *Phys. Rev. Lett.* **119**, 265301 (2017).
- [52] See Supplemental Material at <http://link.aps.org/supplemental/10.1103/PhysRevLett.123.136402> for brief introduction of combining the new method presented in this Letter with the constrained-path AFQMC algorithm.
- [53] B. M. Rubenstein, S. Zhang, and D. R. Reichman, *Phys. Rev. A* **86**, 053606 (2012).
- [54] S. Chandrasekharan and F.-J. Jiang, *Phys. Rev. D* **68**, 091501(R) (2003).
- [55] S. Chandrasekharan and A. C. Mehta, *Phys. Rev. Lett.* **99**, 142004 (2007).
- [56] A. Bazavov, D. Toussaint, C. Bernard, J. Laiho, C. DeTar, L. Levkova, M. B. Oktay, S. Gottlieb, U. M. Heller, J. E. Hetrick, P. B. Mackenzie, R. Sugar, and R. S. Van de Water, *Rev. Mod. Phys.* **82**, 1349 (2010).
- [57] P. Petreczky, *J. Phys. G* **39**, 093002 (2012).
- [58] C. N. Gilbreth, S. Jensen, and Y. Alhassid, *arXiv:1907.10596*.